The Astrophysical Journal Letters, 954:L44 (8pp), 2023 September 10 https://doi.org/10.3847/2041-8213/acf1a2

The Influence of Hydrogen Sulfide on the Optical Properties of Planetary Organic Hazes: Implications for Exoplanet Climate Modeling

Nathan W. Reed, Kevin T. Jansen, Zachary R. Schiffman, Margaret A. Tolbert, and Eleanor C. Browne[1]
Department of Chemistry and the Cooperative Institute of Research in Environmental Sciences, University of Colorado Boulder, Boulder, CO, USA
Received 2023 May 15; revised 2023 August 8; accepted 2023 August 9; published 2023 September 11

Abstract

Planetary organic hazes can play a significant role in influencing a planet's radiative balance and climate, with their impact determined by the optical properties of the haze. The optical properties, in turn, are partly influenced by particle composition. Our previous work, Reed et al., demonstrated that trace amounts of hydrogen sulfide (H_2S) in haze chemistry can substantially affect the haze's composition by generating organosulfur compounds and increasing the amount of organic haze produced. However, no study has measured the optical properties of an H_2S-influenced organic haze. Here we present results from laboratory experiments measuring the real (scattering, n) and imaginary (absorbing, k) refractive indices of haze analogs produced from photochemistry of gas mixtures composed of 0.1% CH_4 and variable H_2S (0–10 ppm_v) in N_2. The optical properties of the aerosol produced were measured in real-time using coupled photoacoustic and cavity ring-down spectroscopy with 405 and 532 nm wavelengths of light. Our findings show that the total extinction of light (scattering plus absorption) by the aerosol increases as a function of H_2S mixing ratio. We provide our best-fit equations for predicting n and k at 405 and 532 nm as a function of the sulfur to carbon molar ratio (S:C) of the precursor gas mixture. Further, we demonstrate how these changes in optical properties could alter the transmittance of 405 and 532 nm light through a haze layer. These results have potential implications for modeling the climate, habitability, and spectra for exoplanets exhibiting organic haze.

Unified Astronomy Thesaurus concepts: Exoplanet atmospheres (487); Optical constants (Dust) (2270); Exoplanet atmospheric composition (2021); Planetary climates (2184); Planetary atmospheres (1244)

1. Introduction

Planetary organic hazes, suspended organic aerosol particles resulting from atmospheric photochemistry, have a significant potential to influence a planet's radiative balance, climate, and spectral appearance (McKay et al. 1991; Hasenkopf et al. 2011; Arney et al. 2016, 2017). Depending on their optical constants, organic hazes may also attenuate UV light, potentially protecting surface life from harmful irradiation and impacting temperature by allowing for the accumulation of greenhouse gases with otherwise short lifetimes (Sagan & Chyba 1997; Pavlov et al. 2001; Wolf & Toon 2010). Thus, it is crucial to understand the optical properties of organic hazes for modeling the climate and habitability of planetary atmospheres, including those of early Earth and exoplanets (Arney et al. 2016, 2017). Additionally, the optical properties of hazes will have an impact on the interpretations of spectral observations of hazy exoplanetary atmospheres, including the potential use of hazes as biosignatures (Arney et al. 2017, 2018).

Several studies have explored the optical properties of organic hazes formed from different gas mixtures and/or by different energy sources (Khare et al. 1984; Hasenkopf et al. 2010; Mahjoub et al. 2012; Ugelow et al. 2017, 2018, 2020; He et al. 2022, 2023; Corrales et al. 2023). However, to date, no study has reported the optical properties of organic hazes that are influenced by sulfur gas photochemistry. Sulfur gas photochemistry is common in planetary atmospheres in the solar system and likely those of exoplanets (Atreya et al. 2003; Hu et al. 2013; Gao et al. 2017). Indeed, sulfur gases have recently been observed in the atmosphere of exoplanet WASP-39b by the JWST Transiting Exoplanet Community Early Release Science Program (Alderson et al. 2023; Rustamkulov et al. 2023; Tsai et al. 2023). Trace amounts of hydrogen sulfide (H_2S), in particular, may coexist with organic haze, especially in reducing atmospheres, which favors haze formation and would allow accumulation of H_2S (Kasting et al. 1989; Kump et al. 2005).

Our previous studies of CH_4 haze photochemistry have shown that the addition of trace amounts of H_2S (0.5–5 ppm_v) to haze precursor gas mixtures significantly impacts organic haze chemistry (Reed et al. 2020, 2022). Specifically, the inclusion of trace H_2S enhances the amount of organic haze aerosol produced, increases aerosol particle effective density, and promotes the formation of organosulfur compounds in the aerosol. Other studies have reported similar results with percent levels of H_2S in non-CH_4 photochemical haze experiments (He et al. 2020; Vuitton et al. 2021).

In addition to changing the chemical properties, trace amounts of H_2S are likely to affect the haze aerosol optical properties. Here we present results from photochemical laboratory experiments measuring the optical properties of organic haze analogs as a function of trace H_2S. Haze analogs were produced by UV photochemistry from precursor gas mixtures consisting of 0.1% CH_4 and variable H_2S in N_2. The scattering, or real (n), and the absorbing, historically called the imaginary (k), refractive indices were determined using coupled photoacoustic and cavity ring-down

[1] Corresponding Author.

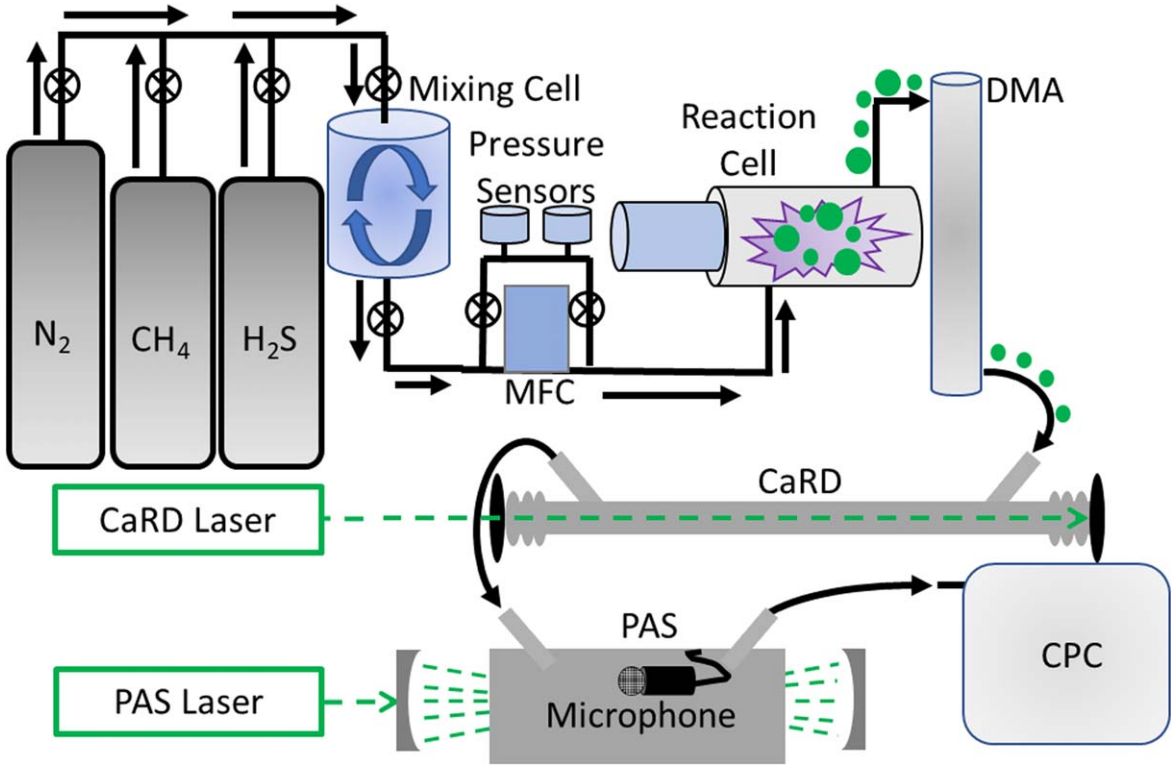

Figure 1. Illustration of flow-through system and aerosol flow in the PASCaRD (PAS coupled with CaRD) instrumentation. "MFC" is "mass flow controller," "DMA" is "differential mobility analyzer," "CaRD" is "cavity ring-down spectroscopy," "PAS" is "photoacoustic spectroscopy," and "CPC" is "condensation particle counter."

(PASCaRD) spectroscopy at 405 and 532 nm. Together, n and k form the complex refractive index (m) and is presented as $m = n + ik$. Our findings indicate that as the mixing ratio of H_2S increases, the aerosol scattering ability (n) increases at both wavelengths studied, and the absorption ability (k) generally increases at the 405 nm wavelength. At 532 nm, k does not vary within measurement error as the S:C ratio is changed. We also demonstrate how such changes in optical properties can influence planetary radiative balance by affecting the transmittance of 405 and 532 nm light through a haze layer.

2. Methods

2.1. Haze Aerosol Generation

Haze aerosol was generated by a flow-through method previously described in detail (Berry et al. 2019; Reed et al. 2020, 2022) and illustrated in Figure 1.

Briefly, gas mixtures consisting of 0.1% CH_4 (Airgas, 99.99%) and variable (0, 1, 5, 7, or 10 ppm_v) H_2S (Airgas, 1000 ppm_v H_2S in N_2) are mixed in a stainless-steel mixing cell with N_2 (Airgas, 99.998%) background gas for at least 8 hr in advance of each experiment. The CH_4 mixing ratio was chosen to be within the range of reduced planetary atmospheres exhibiting a photochemical organic haze (Trainer et al. 2006; Arney et al. 2018) and to be consistent with previous laboratory studies (Ugelow et al. 2017; Reed et al. 2020). The H_2S mixing ratios were chosen to yield a range of sulfur-to-carbon molar ratios (S:C ratio) consistent with S:C emission fluxes of past modeling studies of reduced atmospheres (Domagal-Goldman et al. 2008; Zerkle et al. 2012; Izon et al. 2015, 2017). The CH_4 mixing ratio and S:C ratios are broadly consistent with rocky planets with reducing atmospheres exhibiting organic haze and with either high volcanic activity or biological sulfate reduction (Holland 2002; Archer & Vance 2006; Kump & Barley 2007; Hu et al. 2013).

A mass flow controller (MFC; Millipore, FC-2901 V) set the continuous flow of the precursor gas mixtures from the mixing cell into a stainless-steel reaction cell (volume 300 cm^3) at 100 standard cm^3 per minute (sccm). The reaction cell is equipped with a water-cooled far-UV deuterium lamp (Hamamatsu, L1825) to irradiate the gas mixture, forming haze aerosol products. The lamp has a continuous emission of 115–400 nm, with a peak emission between 115 and 165 nm. The lamp emission includes the Ly-α line at 121.6 nm to mimic the primary wavelength of CH_4 photolysis in reducing atmospheres of the solar system (Smith & Raulin 1999). The steady-state mixing ratio of H_2S after photolysis was measured to be ~57–301 ppb_v (for initial gas mixtures of 1–10 ppm_v, respectively) using gas chromatography sulfur-chemiluminescence detection (GC-SCD). The GC-SCD measurements are described in Appendix A. Aerosol products from the reaction cell flow directly to the PASCaRD system. All experiments are conducted at ambient temperatures (~20°C–25°C) and pressures (~600–610 Torr). To ensure there is no contamination carried over from one experiment to the next, the lamp and reaction cell are disassembled and thoroughly cleaned with acetone and methanol between each experiment. The reaction cell is baked in an oven, and the lamp is allowed to dry before reassembly, and then the system is pumped down by vacuum pumps overnight. In our mass spectrometry measurements (Reed et al. 2020) after an H_2S experiment and after cleaning, we do not observe any S species in the mass spectra of control experiments without H_2S.

2.2. Photoacoustic Spectroscopy and Cavity Ring-down Spectroscopy (PASCaRD)

The PASCaRD system (Figure 1) begins with the flow of aerosol products into a differential mobility analyzer (DMA; TSI, 3081) for size selection based on the electrical mobility diameter of the particles, which was previously found to be independent of the initial H_2S mixing ratio (Reed et al. 2020). Particle sizes are chosen to be larger than the mode diameter of the expected particle size distribution to minimize multiply charged particles. The correction procedure for residual multiply charged particles (between 1% and 7%) has been previously described in detail (Hasenkopf et al. 2010; Zarzana et al. 2012; Ugelow et al. 2017). The size-selected monodisperse particles then flow into the cavity ring-down (CaRD) spectroscopy component. The CaRD, previously described in detail (Freedman et al. 2009; Fuchs et al. 2009), consists of a stainless-steel cavity equipped with highly reflective mirrors at each end. Laser light of either 405 or 532 nm is pulsed into the cavity and is reflected by the mirrors, yielding much longer effective path lengths than the length of the cavity itself. Effective path lengths for 405 and 532 nm lasers are about 12 and 30 km, respectively. The time for the pulse of light to decay to $1/e$ of its original intensity is measured both with (τ, μs) and without (τ_0, μs) haze aerosol present. The extinction (absorption plus scattering) of light (b_{ext}, Mm^{-1}) by aerosol is then calculated as

$$b_{ext} = \frac{R_L}{c}\left(\frac{1}{\tau} - \frac{1}{\tau_0}\right), \tag{1}$$

where c is the speed of light and R_L is the ratio of the mirror-to-mirror length to the length of the cavity that the aerosol occupies ($R_L = 1.13$; Freedman et al. 2009; Fuchs et al. 2009; Ugelow et al. 2017).

Aerosol particles flow from the CaRD to the photoacoustic spectroscopy component (PAS), previously described in detail (Lack et al. 2012; Ugelow et al. 2017). Briefly, the PAS is a resonance cavity equipped with an amplitude-modulated laser at either 405 or 532 nm. Any laser light absorbed by the particles causes the particles to expand and contract at the modulation frequency, producing a pressure wave within the resonance cavity. A calibrated microphone inside the cavity measures the pressure wave, and the signal is converted into an absorption (b_{abs}, Mm^{-1}). Following the PAS, the particles flow into a CPC (TSI, 3022). The CPC measures the particle number density (N, particles cm^{-3}). Particle losses through the PASCaRD system are negligible (Ugelow et al. 2017).

In each experiment, the extinction and absorption of gases is measured by adjusting the DMA diameter to zero; thus no aerosol is transmitted, and only gas-phase species flow into the PASCaRD system. The gas-phase extinction time of τ_0 is thus measured for the CRD measurements, and the gas-phase absorption signals are subtracted as a background from the aerosol measurements in the PAS measurements. The conversion from voltage to absorption is based on a calibration factor from the absorption of an ozone gas standard (Ugelow et al. 2017). To validate PASCaRD measurements and retrieve reliable refractive indices, we use purely scattering (ammonium sulfate) and strongly absorbing (nigrosin dye) standards, as previously described (Hasenkopf et al. 2010; Zarzana et al. 2014; Ugelow et al. 2017).

Extinction (σ_{ext}, cm^2) and absorption (σ_{abs}, cm^2) cross sections are calculated by

$$\sigma_{ext} = \frac{b_{ext}}{N} \times 10^{-8} \tag{2}$$

and

$$\sigma_{abs} = \frac{b_{abs}}{N} \times 10^{-8}, \tag{3}$$

respectively, where the factor of 10^{-8} is for unit conversion. The extinction (Q_{ext}, unitless) and absorption (Q_{abs}, unitless) efficiencies are calculated by

$$Q_{ext} = \frac{4\sigma_{ext}}{\pi D^2} \times 10^{14} \tag{4}$$

and

$$Q_{abs} = \frac{4\sigma_{abs}}{\pi D^2} \times 10^{14}, \tag{5}$$

respectively, where D is the particle mobility diameter (nm) used in the given measurement and 10^{14} is for unit conversion. Hence, Q_{ext} and Q_{abs} are ratios of the extinction and absorption cross sections to the particle geometric cross sections. Note these calculations assume spherical particles due to an absence of information on particle shape.

Real (n) and imaginary (k) refractive index values are determined using a Mie theory code previously detailed (Zarzana et al. 2014; Ugelow et al. 2017). The code evaluates various combinations of n and k to calculate the corresponding extinction and absorption values ($b_{ext,calc}$ and $b_{abs,calc}$). The calculated values are then compared to the experimentally obtained values using the merit function (MF):

$$MF = \frac{1}{N_d}\sum_{i=1}^{N_d}\frac{(b_{ext,i} - b_{ext,calc,i})^2}{b_{ext,i}^2} + \frac{1}{N_d}\sum_{i=1}^{N_d}\frac{(b_{abs,i} - b_{abs,calc,i})^2}{b_{abs,i}^2}, \tag{6}$$

where N_d is the number of particle sizes used in the retrieval. The minimization of the MF is then used to determine the best estimate for n and k.

3. Results and Discussion

3.1. Real and Imaginary Refractive Indices

Figure 2 shows examples of (a) the contour plot of k versus n values with the color indicating the MF value for each combination and (b) the experimentally derived Q_{ext} and Q_{abs} versus particle diameter (square points), along with the calculated fits from Mie theory. The fits in Figure 2(b) demonstrate the consistency between the experimental values and the calculated values from Mie theory, indicating the appropriateness of the best-estimate n and k values. The optical data from Figure 2 is an example from the 0.1% CH_4 and 5 ppm_v H_2S in N_2 experiment at 405 nm. Similar calculations and fits were performed for each S:C ratio studied at both 405 and 532 nm.

Table 1 and Figure 3 show the real (Figure 3(a)) and imaginary (Figure 3(b)) refractive indices of the aerosol as a function of the S:C ratio. The real refractive index, n, increased from 1.5 ± 0.1 to 1.7 ± 0.1 at 532 nm and from 1.4 ± 0.1 to

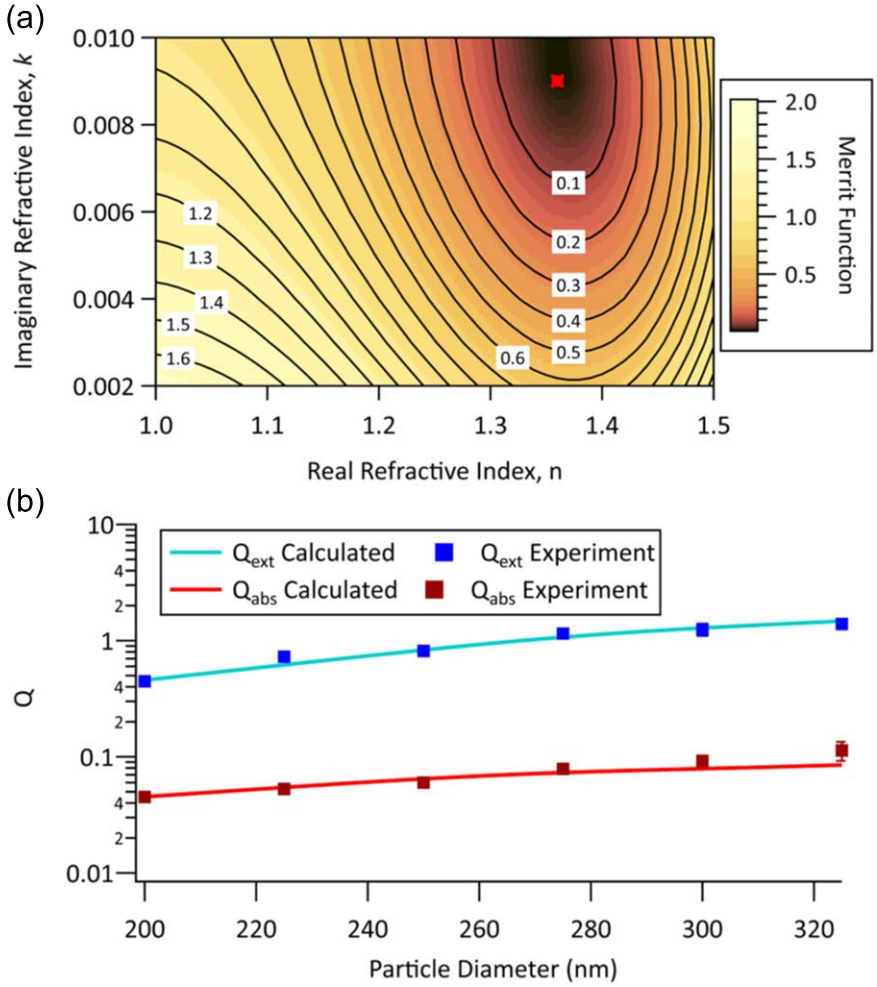

Figure 2. (a) Contour plot of imaginary refractive index (k) values vs. real refractive index (n) values. The color of the contours indicates the MF value calculated for each combination of n and k. The red point represents the best n and k combination to minimize the MF. (b) The experimentally derived Q_{ext} (blue squares) and Q_{abs} (red squares) vs. aerosol particle diameter. The calculated Q_{ext} (solid blue line) and Q_{abs} (solid red line) fits from the Mie theory calculation are included. The data shown are from an example experiment of 0.1% CH_4 and 5 ppm_v H_2S in N_2 experiment at 405 nm.

Table 1
Real (n) and Imaginary (k) Refractive Indices at 405 and 532 nm for Each H_2S Mixing Ratio in Precursor Mixtures of 0.1% CH_4 in N_2

H_2S Mixing Ratio	405 nm		532 nm	
	n	k ($\times 10^{-2}$)	n	k ($\times 10^{-2}$)
No H_2S	1.4 ± 0.1	0.4 ± 0.3	1.5 ± 0.1	$0.2^{+0.3}_{-0.2}$
1 ppm_v	1.3 ± 0.1	0.8 ± 0.3	1.5 ± 0.1	0.2 ± 0.1
5 ppm_v	1.4 ± 0.1	1.3 ± 0.5	1.6 ± 0.1	$0.05^{+0.07}_{-0.05}$
7 ppm_v	1.5 ± 0.1	1.0 ± 0.4	1.7 ± 0.1	0.02 ± 0.02
10 ppm_v	1.6 ± 0.1	1.6 ± 0.6	1.7 ± 0.1	0.13 ± 0.05

1.6 ± 0.1 at 405 nm as a function of the S:C ratio. At 405 nm, there is a general increase in k from $0.4 \times 10^{-2} \pm 0.3 \times 10^{-2}$ to $1.6 \times 10^{-2} \pm 0.6 \times 10^{-2}$. At 532 nm, k does not change within measurement error as a function of S:C ratio. The increase in the total extinction is therefore dominated by scattering rather than absorption at 532 nm, but absorption at 405 nm increased as a function of the S:C ratio. Using linear least-squares fitting, the values of n and k as a function of the S:C ratio can be predicted by: $n_{405} = (1.30 \pm 0.02) + (28 \pm 3)(\text{S:C})$, $n_{532} = (1.48 \pm 0.02) + (24 \pm 5)(\text{S:C})$, and $k_{405} = (0.006 \pm 0.002) + (1.0 \pm 0.3)(\text{S:C})$. Note the best-fit equations for n and k as a function of the S:C ratio should be applied only to reducing atmospheres, with H_2S and CH_4 as the sulfur and carbon sources.

Note that most of the uncertainty in the n and k values comes from experiment-to-experiment variability, likely caused by minor differences in lamp intensity and perhaps, to a lesser extent, minor differences in precursor mixtures of repeat experiments. Two experiments were performed for each precursor mixture. The other source of uncertainty comes from the n and k retrievals. Uncertainty in n and k retrievals comes from a Monte Carlo simulation of many iterations of the Mie code described previously (Jansen 2023). Based on the variability from experiment-to-experiment of repeats (from 0.5% to 6.5%) and the uncertainties from retrievals (from 1.2% to 7%), we used a conservative uncertainty of ± 0.1 ($\sim$7%) to all n values. For the k values, based on the variability from experiment-to-experiment (from 0.09% to 141%) and the uncertainty in the retrievals (from 0% to 34%), we used either an uncertainty of 35% or used the variability between repeat experiments as the uncertainty, whichever was greater. Since negative values are unphysical, asymmetric errors are given in cases where zero values are within error.

An increase in n as a function of H_2S is consistent with the findings in our previous work (Reed et al. 2020), which showed

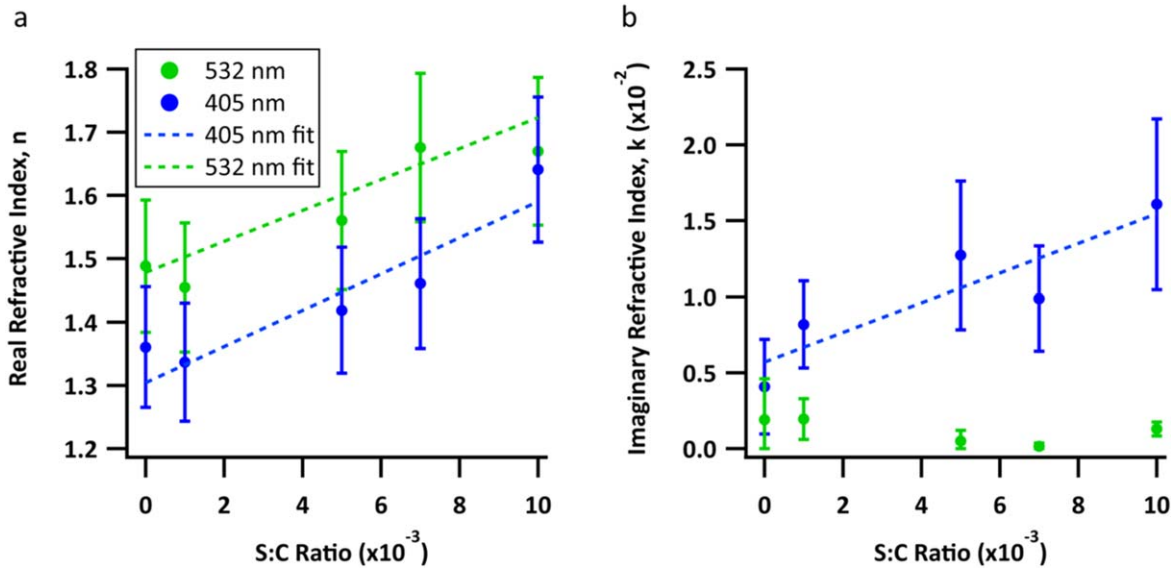

Figure 3. (a) Real refractive indices, n and (b) imaginary refractive indices, k, as a function of the S:C ratio of the initial gas mixture at both 405 nm (blue) and 532 (green) nm. Each point is the average of two different measurements. Error bars are described in Section 3.1. Dotted lines represent linear least-squares best-fit lines for the data.

evidence for the significant production of thiols and sulfides in organic haze particles when trace H_2S was included in the precursor mixtures. Reed et al. (2020) proposed that the thiyl radical, formed from photolysis of H_2S, reacts with unsaturated alkenes, produced from CH_4 haze chemistry, leading to the formation of thiols and sulfides. This chemistry is analogous to thiol-ene click chemistry used in sulfide polymer synthesis. Polymer systems cross-linked with sulfides are desirable in materials research as materials of high-refractive indices ($>\sim$1.6; Chan et al. 2009; Bhagat et al. 2012; Mavila et al. 2021). The high-refractive index of sulfides is thought to be due to what is called the high "molar refractivity" and high polarizability of sulfur atoms. Further, the increase in n is also consistent with the observed increase in particle effective density as a function of H_2S mixing ratio from our previous work (Reed et al. 2020). Effective density is related to the material density, as well as factors such as sphericity and porosity (DeCarlo et al. 2004; Liu & Daum 2008). Ugelow et al. (2018) also observed an increase in n along with particle effective density in similar studies as a function of trace O_2 (Ugelow et al. 2018). The reason for the increase of k at 405 nm as a function of S:C ratio is unclear. However, it is reasonable to assume the increased production of absorbing molecules, such as the same thiols and sulfides previously mentioned.

4. Impact of Changing Refractive Indices on Transmittance through an Aerosol Layer

To provide context on the sensitivity of visible light transmission to the variation of the haze optical properties measured here, we present a simplified calculation of the total transmittance through an aerosol layer for 405 and 532 nm radiation. The transmittance is calculated using Equation (7):

$$T = 1 - R - A, \tag{7}$$

where R is the reflectance and is defined as $R = 2\beta\tau_{sca}$ and A is the absorbance and is defined as $A = 2\tau_{abs}$. Here, β is the up-scattering fraction, or the fraction of light scattered back into space, and τ_{sca} and τ_{abs} are the scattering and absorption optical depths, respectively (Chylek & Wong 1995). For simplicity, we set β to 0.5 and thus assume isotropic scattering. We used our experimentally determined values of n and k and Mie theory to calculate the aerosol scattering and absorption cross sections assuming 100 nm diameter particles. We chose a column density of 6×10^{10} cm^{-2}. This value produces a zero transmittance at 405 nm assuming the Khare et al. (1984) optical constants discussed below (a complete anti-greenhouse scenario) and provides dynamic range for the other scenarios. The scattering and absorbing optical depths are calculated as the product of the column density and the appropriate cross section.

Figure 4(a) shows transmittance for each S:C ratio investigated. Note the errors for the n and k values are not propagated into the transmittance calculations as the data presented here are meant to be qualitative and illustrative of trends rather than focused on exact numerical values. The transmittance of 405 and 532 nm light generally decreases as the S:C ratio increases. It is also apparent that the decrease in transmittance at 405 nm is more sensitive to the S:C ratio than the transmittance at 532 nm. From an S:C ratio of 0 to 0.01, the transmittance decreases by a factor of $\sim$8.3 at 405 nm and by a factor of $\sim$1.1 at 532 nm. This trend is due to the increasing absorption at 405 nm as the S:C ratio increases.

The calculated transmittance assumes the same column density for all cases. However, our previous work showed that organic haze particle production greatly increases with increasing inclusion of trace H_2S (Reed et al. 2020). The effect of increasing levels of trace H_2S on organic haze transmittance of light is therefore twofold: each particle attenuates more light, and more particle mass is produced.

Figure 4(b) shows the transmittance calculated using the n and k values of four similar studies: Hasenkopf (2010), Ugelow et al. (2017, 2018), and Khare et al. (1984). Except for Khare et al. (1984), each of these studies used a precursor gas mixture of 0.1% CH_4 in N_2 but with various haze generation and refractive index retrieval methods (detailed in Appendix B). Khare et al. (1984) used 1% CH_4 in N_2 and is included in our

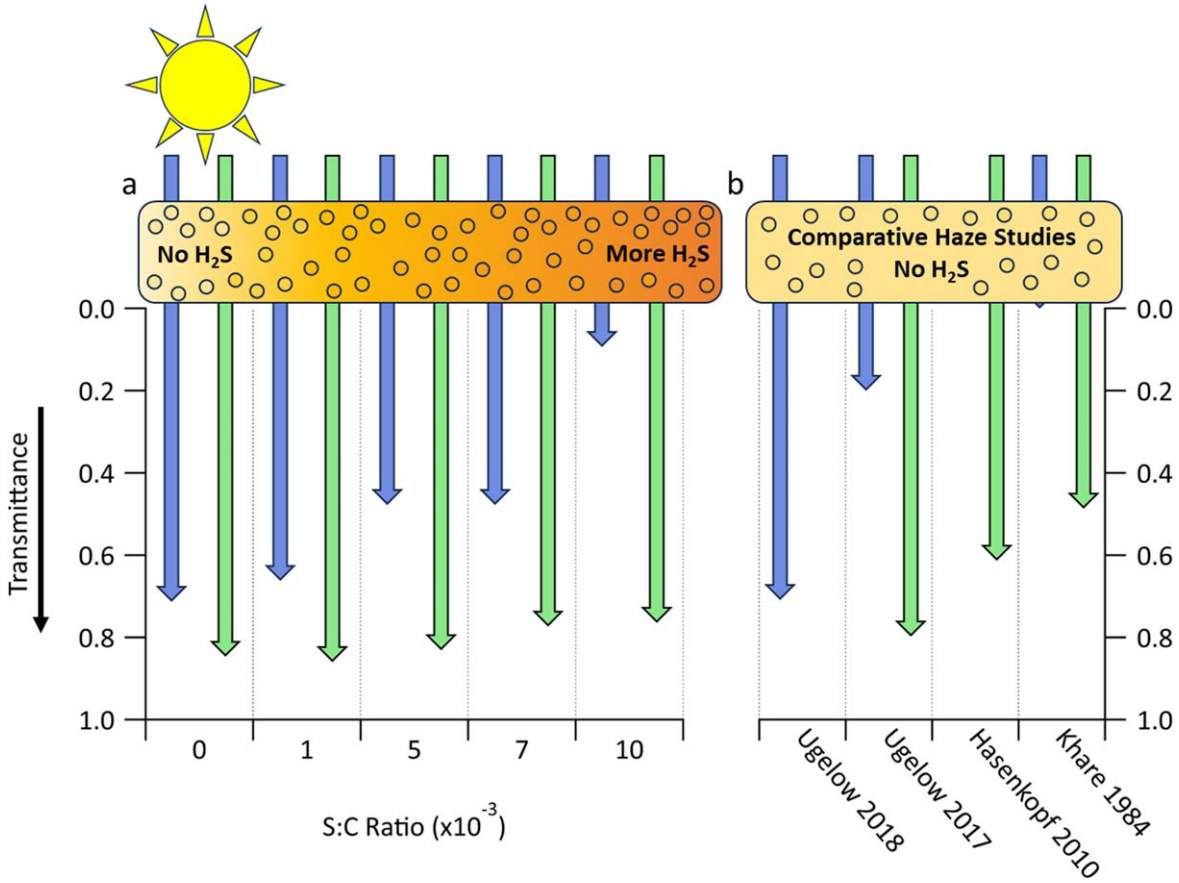

Figure 4. The calculated transmittance of 405 (blue arrows) and 532 (green arrows) nm light vs. (a) the S:C ratio and (b) the comparative studies. The comparative studies measured the optical properties of haze generated from 0.1% CH_4 in N_2, except for Khare et al. (1984), which used 1% CH_4 in N_2. Values from Khare et al. (1984) were taken from comparable wavelengths (413.3 and 563.5 nm). Ugelow et al. (2017) and Khare et al. (1984) produced haze analogs using spark and direct current (D.C.) discharge, respectively, rather than photochemically. Ugelow et al. (2018) only measured at 405 nm and Hasenkopf et al. (2010) only measured at 532 nm.

comparisons as it is a seminal study in haze optical properties. The three comparative studies that produced organic haze analogs from precursor mixtures of 0.1% CH_4 in N_2 (Ugelow et al. 2017, 2018; Hasenkopf et al. 2010) had variations between their reported optical constants leading to differences in the calculated transmittance (by a factor of ∼3.6 for the 405 nm cases and ∼1.3 for the 532 nm cases). The variations in the transmittance as a function of trace H_2S span the range of variations across the comparative studies. Although the Khare et al. (1984) optical constants are widely used for models and calculations of hazes, it is clear from the plot that differences in optical constants can greatly impact important spectral, climate, and radiative factors of interest in planetary models. Beyond precursor gas composition, the variations between studies could be due to different methods of aerosol generation (UV lamp, spark discharge, or D.C. discharge), the form of the analog sample (aerosol or film), and methods of measurement (PASCaRD, CaRD-only, or spectrophotometry).

Not shown in this comparison are optical constants derived from different gas mixtures, which also show variability. For example, it has been demonstrated that haze optical properties are highly sensitive to oxygen-containing precursor gases, including CO_2 (Corrales et al. 2023), H_2O (He et al. 2023), and O_2 (Ugelow et al. 2018). Generally, it has been observed that n and k values increase with increasing mixing ratios of oxygen-containing precursor gases at or near visible wavelengths (Ugelow et al. 2018; Corrales et al. 2023; He et al. 2023). Therefore, we emphasize the importance of carefully choosing optical constants available in the literature for atmospheric and climate models of organic haze. Factors such as aerosol production and measurement methods of a given study should be considered along with the composition of the haze aerosol and its source gases.

5. Conclusion

We have shown that the addition of increased H_2S to CH_4 haze chemistry increases the extinction of light at the optical wavelengths of 405 and 532 nm, driven by both scattering and absorption at 405 nm and scattering at 532 nm. The findings of this study have significant implications for modeling planetary climate and habitability of exoplanets exhibiting organic haze. The optical constants extracted from this study can aid in the interpretation of exoplanetary haze spectra (Arney et al. 2017, 2018; Corrales et al. 2023; He et al. 2023). Moreover, since H_2S is both a volcanic gas and emitted biologically, constraints on volcanic activity and, potentially, biosignatures on exoplanets, may be more informed using the optical properties of a H_2S-inluenced haze in an exoplanet's spectrum.

Acknowledgments

This work was supported by NASA grant 80NSSC20K0232. N.R. was supported in part by the University of Colorado Boulder Department of Chemistry 2022 Sharrah Fellowship.

Z.R.S. was supported in part by the CIRES Graduate Student Research Award and the NOAA Cooperative Agreement with CIRES, NA17OAR4320101, as well as NSF grant AGS 1925191. We would like to thank Randall Shearer for providing the GC-SCD measurements and expertise.

Data Availability

All data and the Mie code software program are archived and made available through the CU Scholar Data Repository provided by the University Libraries at the University of Colorado, Boulder.

Software and code are available at doi:10.25810/2ssz-5649.

All data, including raw data, are available at doi:10.25810/tem1-ab24.

Appendix A
Description of Gas Chromatograph-sulfur Chemiluminescence Detection (GC-SCD) Experiments

Two separate gas samples were extracted from the reaction cell using a gas-tight syringe: one before the lamp was turned on (lamp-off sample) and one after 20–30 minutes of UV lamp irradiation (lamp-on sample). A given sample was then injected into an HP 5890 series II gas chromatograph with a split injector (1:10 split ratio) and a 44 m Restek MXT-1 micron film column. The detector was an SCD model 350B with an Agilent duel purpose (DP) upgrade. A peak in the chromatograms at ∼0.6 minutes was verified to be H_2S by comparison to a standard. Using the known initial H_2S mixing ratio, the peak area of H_2S from the lamp-off sample was used to calculate a scaling factor that converts the H_2S peak area from the lamp-on sample into a mixing ratio. The lamp-on mixing ratios for the 1, 5, 7, and 10 ppm_v precursor mixing ratios were calculated to be 57, 232, 270, and 301 ppb_v, respectively.

Appendix B
Table of Organic Haze Optical Constants from the Literature

The optical constants retrieved for the control experiments (i.e., hazes formed with 0.1% CH_4 in N_2 without H_2S) can be compared to those presented in the literature. Table B1 compiles the optical constants of laboratory hazes presented in this study and other studies in the literature using a starting gas mixture of 0.1% CH_4 in N_2.

Table B1
Literature Value Optical Constants of Hazes Produced from 0.1% CH_4 in N_2[a]

Study	405 nm		532 nm	
	n	k ($\times 10^{-2}$)	n	k ($\times 10^{-2}$)
This Study	1.4 ± 0.1	0.4 ± 0.3	$1.5 \pm .1$	$0.2^{+0.3}_{-0.2}$
Ugelow et al. (2018)[b]	1.40 ± 0.02	0.2 ± 0.1	⋯	⋯
Ugelow et al. (2017)[c]	1.66 ± 0.03	0.8 ± 0.2	1.56 ± 0.02	0.3 ± 0.1
Hasenkopf et al. (2010)[d]	⋯	⋯	1.35 ± 0.01	2.3 ± 0.7
Khare et al. (1984)[e]	1.69	7.6	1.70	2.3

Notes.

[a] Khare et al. (1984) used 1% CH_4 in N_2, not 0.1% CH_4 in N_2. The data were included here, though, as this is an often-cited study.

[b] From Table 1 of Ugelow et al. (2018) for the 0.1% CH_4/N_2 case.

[c] Haze produced using spark discharge.

[d] Measured using only CaRD.

[e] Measured using spectrophotometry Brewster angle method on haze films produced from D.C. discharge. Comparable wavelengths used were 413.3 nm (to compare to 405 nm) and 563.5 nm (to compare to 532 nm).

ORCID iDs

Nathan W. Reed https://orcid.org/0000-0002-0401-5993
Kevin T. Jansen https://orcid.org/0000-0002-5142-6808
Zachary R. Schiffman https://orcid.org/0000-0002-7240-4739
Margaret A. Tolbert https://orcid.org/0000-0001-5730-6412
Eleanor C. Browne https://orcid.org/0000-0002-8076-9455

References

Alderson, L., Wakeford, H. R., Alam, M. K., et al. 2023, Natur, 614, 664
Archer, C., & Vance, D. 2006, Geo, 34, 153
Arney, G., Domagal-Goldman, S. D., Meadows, V. S., et al. 2016, AsBio, 16, 873
Arney, G., Domagal-Goldman, S. D., & Meadows, V. S. 2018, AsBio, 18, 311
Arney, G. N., Meadows, V. S., Domagal-Goldman, S. D., et al. 2017, ApJ, 836, 49
Atreya, S. K., Mahaffy, P. R., Niemann, H. B., Wong, M. H., & Owen, T. C. 2003, P&SS, 51, 105
Berry, J. L., Ugelow, M. S., Tolbert, M. A., & Browne, E. C. 2019, ApJL, 885, L6
Bhagat, S. D., Chatterjee, J., Chen, B., & Stiegman, A. E. 2012, MaMol, 45, 1174
Chan, J. W., Zhou, H., Hoyle, C. E., & Lowe, A. B. 2009, Chem Mater, 21, 1579
Chylek, P., & Wong, J. 1995, GeoRL, 22, 929
Corrales, L., Gavilan, L., Teal, D. J., & Kempton, E. M. R. 2023, ApJL, 943, L26
DeCarlo, P. F., Slowik, J. G., Worsnop, D. R., Davidovits, P., & Jimenez, J. L. 2004, AerST, 38, 1185
Domagal-Goldman, S. D., Kasting, J. F., Johnston, D. T., & Farquhar, J. 2008, E&PSL, 269, 29
Freedman, M. A., Hasenkopf, C. A., Beaver, M. R., & Tolbert, M. A. 2009, JPCA, 113, 13584
Fuchs, H., Dube, W. P., Wagner, N. L., Williams, E. J., & Brown, S. S. 2009, EnST, 43, 7831
Gao, P., Marley, M. S., Zahnle, K., Robinson, T. D., & Lewis, N. K. 2017, AJ, 153, 139
Hasenkopf, C. A., Beaver, M. R., Trainer, M. G., et al. 2010, Icar, 207, 903
Hasenkopf, C. A., Freedman, M. A., Beaver, M. R., Toon, O. B., & Tolbert, M. A. 2011, AsBio, 11, 135
He, C., Hörst, S. M., Lewis, N. K., et al. 2020, NatAs, 4, 986
He, C., Hörst, S. M., Radke, M., & Yant, M. 2022, PSJ, 3, 25
He, C., Radke, M., Moran, S. E., et al. 2023, arXiv:2301.02745
Holland, H. D. 2002, GeCoA, 66, 3811
Hu, R., Seager, S., & Bains, W. 2013, ApJ, 769, 6
Izon, G., Zerkle, A. L., Williford, K. H., et al. 2017, PNAS, 114, E2571
Izon, G., Zerkle, A. L., Zhelezinskaia, I., et al. 2015, E&PSL, 431, 264
Jansen, K. J. 2023, PhD Thesis, Univ. of Colorado
Kasting, J. F., Zahnle, K. J., Pinto, J. P., & Young, A. T. 1989, OLEB, 19, 95
Khare, B. N., Sagan, C., Arakawa, E. T., et al. 1984, Icar, 60, 127
Kump, L. R., & Barley, M. E. 2007, Natur, 448, 1033
Kump, L. R., Pavlov, A., & Arthur, M. A. 2005, Geo, 33, 397
Lack, D. A., Langridge, J. M., Bahreini, R., et al. 2012, PNAS, 109, 14802
Liu, Y., & Daum, P. H. 2008, JAerS, 39, 974
Mahjoub, A., Carrasco, N., Dahoo, P. R., et al. 2012, Icar, 221, 670
Mavila, S., Sinha, J., Hu, Y., et al. 2021, ACS Appl Mater Interfaces, 13, 15647
McKay, C. P., Pollack, J. B., & Courtin, R. 1991, Sci, 253, 1118
Pavlov, A. A., Brown, L. L., & Kasting, J. F. 2001, JGRE, 106, 23267
Reed, N. W., Browne, E. C., & Tolbert, M. A. 2020, ESC, 4, 897
Reed, N. W., Wing, B. A., Tolbert, M. A., & Browne, E. C. 2022, GeoRL, 49, e97032
Rustamkulov, Z., Sing, D. K., Mukherjee, S., et al. 2023, Natur, 614, 659
Sagan, C., & Chyba, C. 1997, Sci, 276, 1217
Smith, N. S., & Raulin, F. 1999, JGRE, 104, 1873
Trainer, M. G., Pavlov, A. A., DeWitt, H. L., et al. 2006, PNAS, 103, 18035

Tsai, S. M., Lee, E. K. H., Powell, D., et al. 2023, Natur, 617, 483
Ugelow, M. S., Berry, J. L., Browne, E. C., & Tolbert, M. A. 2020, AsBio, 20, 658
Ugelow, M. S., De Haan, D. O., Hörst, S. M., & Tolbert, M. A. 2018, ApJL, 859, L2
Ugelow, M. S., Zarzana, K. J., Day, D. A., Jimenez, J. L., & Tolbert, M. A. 2017, Icar, 294, 1
Vuitton, V., Moran, S. E., He, C., et al. 2021, PSJ, 2, 2
Wolf, E. T., & Toon, O. B. 2010, Sci, 328, 1266
Zarzana, K. J., Cappa, C. D., & Tolbert, M. A. 2014, AerST, 48, 1133
Zarzana, K. J., De Haan, D. O., Freedman, M. A., Hasenkopf, C. A., & Tolbert, M. A. 2012, EnST, 46, 4845
Zerkle, A. L., Claire, M. W., Domagal-Goldman, S. D., Farquhar, J., & Poulton, S. W. 2012, NatGe, 5, 359